PIER C

A Novel Bandpass-to-All-Stop Switchable Absorptive Filter with Ultra-Wideband Reflectionless Range

Bingjie Yang[1], Zhongbao Wang[1, 2, *], Shipeng Zhao[1], Hongmei Liu[1],
Mingming Gao[1, 2], and Shaojun Fang[1]

[1]*School of Information Science and Technology, Dalian Maritime University, Dalian 116026, Liaoning, China*
[2]*Liaoning Key Laboratory of Radio Frequency and Big Data for Intelligent Applications, Liaoning Technical University
Huludao 125105, Liaoning, China*

ABSTRACT: A novel bandpass-to-all-stop switchable absorptive filter with an ultra-wideband reflectionless range is proposed in this paper. The bandpass section of the filter consists of a dual-mode resonator and two L-shaped feeding lines. The dual-port reflectionless characteristic is achieved by loading absorption networks at the end of the open stubs of the feeding lines, which are composed of two parallel coupled lines and absorption resistors. The switching of the reflectionless bandpass filter (RBPF) to the all-stop filter (ASF) is realized by controlling the on/off behavior of the PIN diode through the bias voltage. Measurements show that the filter prototype at the center frequency of 2.43 GHz with the 3-dB fractional bandwidth (FBW) is 8.23%. For the RBPF state, the filter has an ultra-wideband reflectionless FBW of 214% and upper stopband rejection better than 33 dB up to 6 GHz. Besides, the rejection is better than 30 dB from 0 to 5.32 GHz in the ASF state.

1. INTRODUCTION

In recent years, with the rapid development of wireless communication systems, it is necessary to design more multifunction microwave devices to reduce the size of the RF front-end. As an important component of the RF front-end, switchable/tunable filters have attracted widespread attention [1, 2]. Switchable/tunable filters can be achieved through PIN diodes [3, 4], RF-MEMS switches [5], single-pole multi-throw switches [6, 7], semiconductor varactor diodes [8], etc. However, most switchable/tunable filters are reflective filters, which can potentially introduce problems such as efficiency loss and dynamic range loss.

Conventional reflective microwave filters reflect out-of-band signals directly back to the source, which may cause deterioration in system performance. Reflectionless filters have received increasing attention, which can absorb out-of-band reflected energy to increase the signal-to-noise ratio. The most common approach to achieve out-of-band reflectionlessness is to load absorption networks at the ports of conventional bandpass filters (BPFs) [9, 10], which is simple to implement and has a compact size. In [9], the proposed quasi-absorptive filter consists of a bandpass section and an absorptive section (a quarter-wavelength shorted transmission line with matched resistors in series), which can be designed to an arbitrarily high order. In [10], a reflectionless balanced bandpass filter is realized using a three-line coupling structure and an absorbing section, and it has common-mode suppression characteristics. Reflectionless filters designed based on diplexer architecture are another dominant design option today [11–13]. This

design approach allows for a wider range of reflectionless behavior. In [11], band-pass and band-stop filter channels with complementary transfer functions are designed, which dissipate the input energy not transmitted by one branch with the loaded resistor of the other channel. In addition, many reflectionless band-pass filters (RBPFs) based on balanced circuits have been proposed [14, 15].

Further, attempts have been made to combine tunable/switchable band-pass filters with reflectionless characteristics. Various design methods for designing tunable RBPFs have been reported [16, 17]. In [16], a tunable reflectionless BPF is realized using two quadrature couplers and two reflective BPFs. However, the insertion loss (IL) is large, and the reflectionless bandwidth (BW) is narrow. In [17], a frequency and bandwidth tunable RBPF is implemented using a design methodology that relies on the transformation of a normalized low-pass filter prototype to a band-pass filter prototype. However, reports on switchable reflectionless filters are relatively scarce. Most of the switchable filters ignore the adverse effects of out-of-band signals on the stability of the RF system. In [18], a class of tunable band-pass filters that can be switched to an all-stop filter (ASF) was reported. However, only the input reflectionless characteristic is realized. In [19], a switchable filter with two modes of operation, an RBPF, and a reflectionless band-stop filter is proposed. However, its reflectionless range is narrow, and its out-of-band rejection performance is poor.

Based on the above issues, a novel bandpass-to-all-stop switchable absorptive filter with an ultra-wideband reflectionless range is proposed in this paper. The switchable absorptive filter consists of a band-pass section (a dual-mode resonator

---

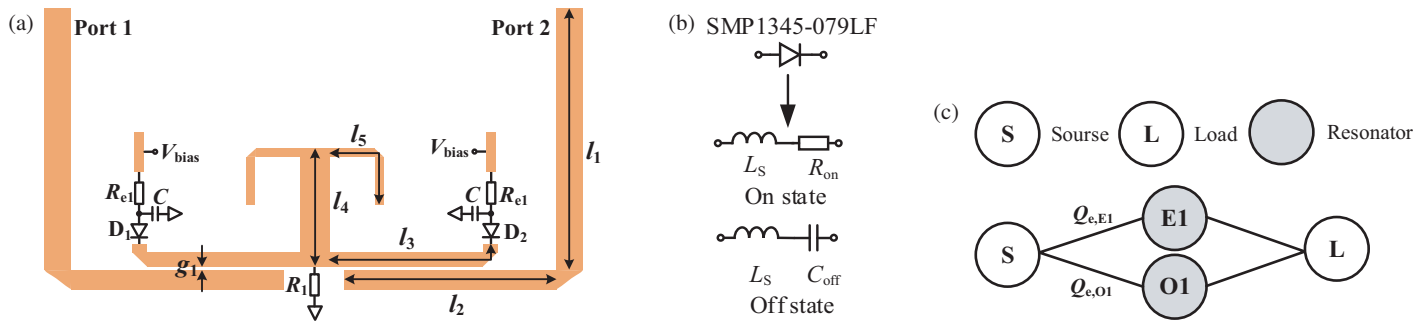* Corresponding author: Zhongbao Wang (wangzb@dlmu.edu.cn).

FIGURE 1. (a) Layout of the initial switchable BPF. (b) Equivalent circuit model of PIN diode. (c) Coupling topology.
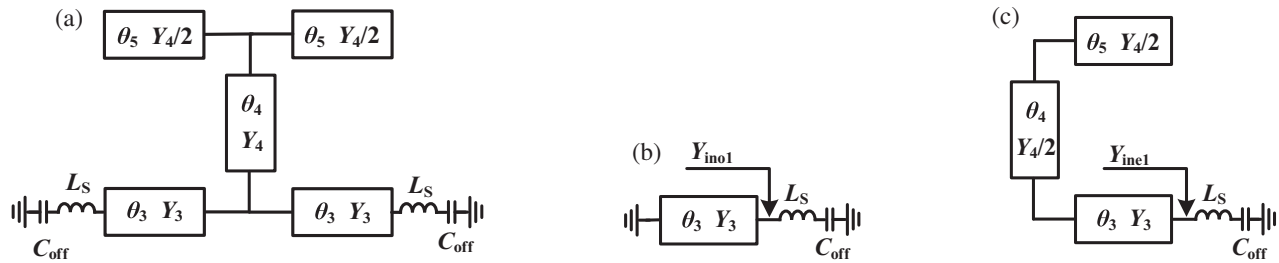

FIGURE 2. (a) Schematic of the DMR with reverse-biased diodes. (b) Odd-mode excitation. (c) Even-mode excitation.

(DMR) loaded with a grounding resistor), two absorption networks (two parallel coupled line stubs with absorption resistors connected at the open stub end), and two L-shaped feeding lines. The switching from RBPF to ASF is realized by controlling the PIN diodes loaded at the open end of the resonator. It combines the following features: 1) Two operating states: RBPF and ASF. 2) Dual-port reflectionless behavior and ultra-wide reflectionless range in the RBPF state. 3) Wide stopband characteristics in RBPF state.

2. THEORETICAL ANALYSIS AND DESIGN PROCEDURE

2.1. Design of Switchable Filter

Figure 1(a) depicts the circuit structure of the initial switchable filter. The band-pass section consists of a DMR loaded with a grounding resistor R_1 and two L-shaped feeding lines. PIN diodes D_1 and D_2 loaded at the end of the open stubs of the resonator are used to control the on/off behavior of the BPF. The model number of the PIN diode was chosen to be the Skyworks product SMP1345-079LF, whose equivalent circuit is given in Fig. 1(b) [6]. In this case, L_s is the parasitic inductance of 0.7 nH; R_{on} is the forward-biased resistance of 2 Ω; and C_{off} is the reverse-biased capacitance with a value of 0.15 pF. The capacitor $C = 100$ pF is used to bypass the RF signal and block the DC voltage. The current-limiting resistor $R_{e1} = 2$ kΩ controls the on/off of the PIN diode in conjunction with the external bias voltage V_{bias}. Fig. 1(c) illustrates the coupling topology of the BPF. Node S and node L denote the source and load. E1 and O1 represent the even and odd resonant modes of the DMR, respectively, and there is no coupling between these two resonant modes.

The schematic of the DMR is shown in Fig. 2(a). The characteristic admittance of each branch is represented by Y_i, and its electrical length is represented by θ_i. When the diodes D_1 and D_2 loaded at the open end of the resonator are reverse-biased, the DMR is in operation. At this time, the diodes are equivalent to an inductor L_S and a capacitor C_{off} in series. Since the capacitance effect due to the reverse-biased diodes causes a shift in the resonant frequency, it needs to be taken into account when the resonator is analyzed.

Since the resonator is symmetrical, its resonant characteristics can be discussed using the method of odd-even mode analysis. The equivalent circuits of the DMR in odd and even modes are given in Fig. 2(b) and Fig. 2(c), respectively. Therefore, the input admittances Y_{ino1} and Y_{ine1} can be expressed as

$$Y_{ino1} = -jY_3 \cot\theta_3 + \frac{j\omega C_{off}}{1 - \omega^2 L_s C_{off}} \tag{1}$$

$$Y_{ine1} = jY_3 \frac{2Y_3\tan\theta_3 + Y_4\tan(\theta_4 + \theta_5)}{2Y_3 - Y_4\tan\theta_3\tan(\theta_4 + \theta_5)} + \frac{j\omega C_{off}}{1 - \omega^2 L_s C_{off}} \tag{2}$$

The odd-mode resonant frequency f_{0o1} and even-mode resonant frequency f_{0e1} can be determined from $\text{Im}(Y_{ino1}) = 0$ and $\text{Im}(Y_{ine1}) = 0$, respectively.

From Equations (1) and (2), it can be seen that odd-mode resonant frequency f_{0o1} is determined by the electrical length θ_3, and even-mode resonant frequency f_{0e1} depends on the electrical lengths θ_3, θ_4, and θ_5. Fig. 3 exhibits the effect of the resonator's branch length on the odd- and even-mode frequencies l_3 and l_5 respectively corresponding to θ_3 and θ_5 in Fig. 2(a). The following conclusions can be obtained: $f_{0e1} > f_{0o1}$. f_{o1} is only controlled by l_3, and changing l_3 has a greater effect on f_{0o1} than on f_{0e1}. f_{0e1} is affected by all the stubs. In the simulation, first adjust l_3 to meet the odd-mode resonant frequency
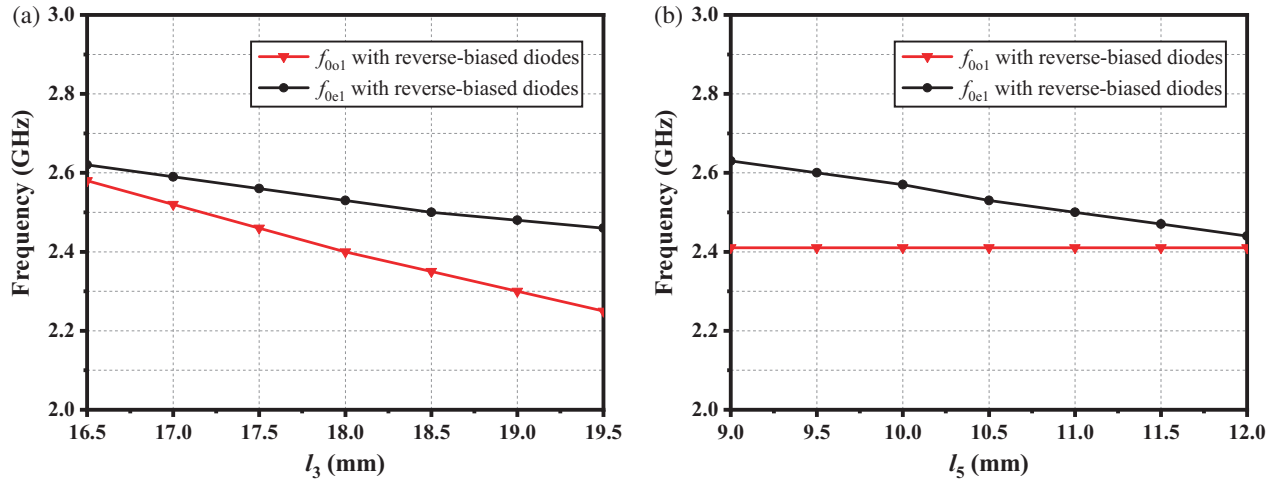
FIGURE 3. Effect of (a) l_3 and (b) l_5 on the odd- and even-mode resonant frequencies of the DMR loaded with reverse-biased diodes.
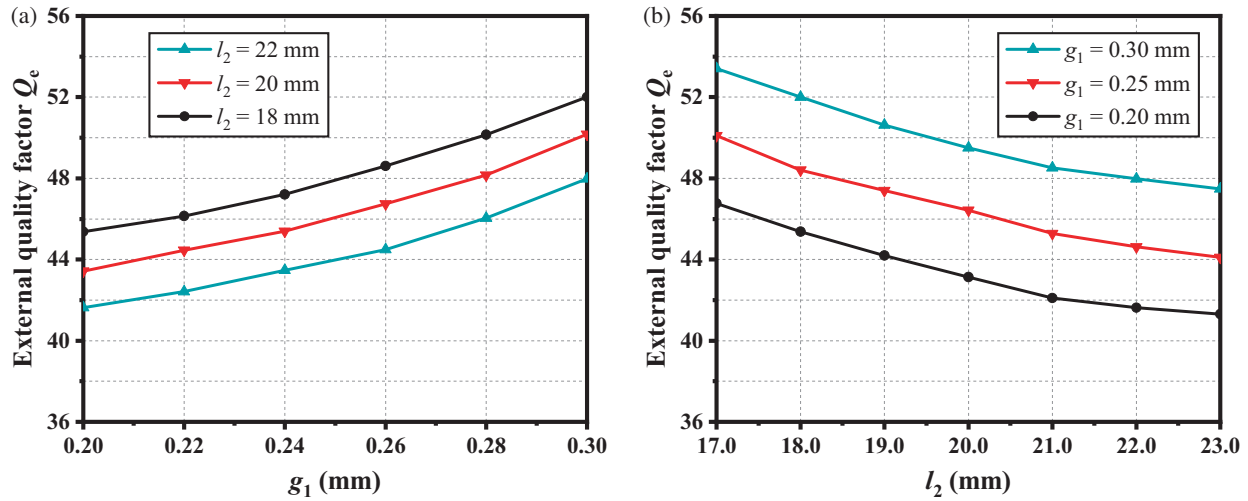

FIGURE 4. The relationship between external quality factor Q_e and (a) g_1 with different l_2, (b) l_2 with different g_1.

f_{0o1} and then adjust the other stubs to determine the even-mode resonant frequency f_{0e1}.

According to the coupling topology in Fig. 1(c), since there is no coupling between the first two resonant modes of the DMR, the normalized coupling matrix can be expressed as (3)

$$[m] = \begin{bmatrix} 0 & m_{S1} & m_{S2} & 0 \\ m_{S1} & m_{11} & 0 & m_{1L} \\ m_{S2} & 0 & m_{22} & m_{2L} \\ 0 & m_{1L} & m_{2L} & 0 \end{bmatrix} \quad (3)$$

where m_{Si} represents the coupling strength between the input feeding line and the resonator, and m_{iL} represents the coupling strength between the output feeding line and the resonator. m_{ii} represents the self-coupling coefficient of mode i ($i = 1, 2$). The required external quality factors and self-resonant frequency can be evaluated by [20]

$$Q_{ei} = \frac{1}{m_{Si}^2 \cdot \text{FBW}} \quad (4)$$

$$f_{0i} = f_0 \left(1 - \frac{m_{ii} \cdot \text{FBW}}{2} \right) \quad (5)$$

Then, a two-order BPF with the center frequency of 2.45 GHz, BW of 200 MHz, and return loss (RL) better than 20 dB is designed. The coupling matrix can be synthesized as (6)

$$[m] = \begin{bmatrix} 0 & -0.678 & 0.443 & 0 \\ -0.678 & 0.44 & 0 & 0.678 \\ 0.443 & 0 & -0.91 & 0.443 \\ 0 & 0.678 & 0.443 & 0 \end{bmatrix} \quad (6)$$

According to the targeted index, $f_{0o1} = 2.406$ GHz, $f_{0e1} = 2.543$ GHz, $Q_{e,O1} = 26.65$, $Q_{e,E1} = 62.42$ can be calculated. Based on the analysis of the DMR f_{0o1} and f_{0e1} can be satisfied by adjusting the length of each stub of the DMR. The coupling gap and feeding line length affect the external quality factor Q_e. Its value is determined by $Q_e = (Q_{e,E1} + Q_{e,O1})/2$ [6]. Figs. 4(a) and 4(b) show the variation of Q_e with the changes of g_1 and l_2. It can be found that the external quality factor Q_e
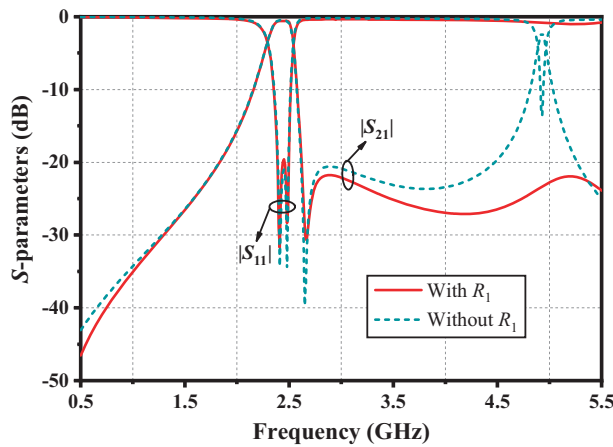
FIGURE 5. Simulated performances of the BPF with or without grounding resistor R_1.

increases as the coupling gap g_1 increases, and the feeding line length l_2 decreases.

In order to suppress the even harmonics generated near 4.9 GHz, the grounding resistor $R_1 = 50\,\Omega$ is loaded in the center of the DMR. It can be seen from Fig. 5 that the second harmonic is well suppressed after loading the grounding resistor R_1. Furthermore, it is worth mentioning that the filtering response of the passband is almost unaffected.

When the diodes D_1 and D_2 loaded on the resonator are forward-biased, the equivalent is an inductor L_s in series with a resistor R_{on}. Fig. 6(a) illustrates the equivalent circuit of the resonator. The odd-mode equivalent circuit and even-mode equivalent circuit are shown in Figs. 6(b) and 6(c), respectively. The odd-mode and even-mode input admittances are expressed as

$$Y_{\text{ino2}} = -jY_3 \cot\theta_3 + \frac{R_{\text{on}} - j\omega L_s}{R_{\text{on}}^2 + \omega^2 L_s^2} \tag{7}$$

$$Y_{\text{ine2}} = jY_3 \frac{2Y_3 \tan\theta_3 + Y_4 \tan(\theta_4+\theta_5)}{2Y_3 - Y_4 \tan\theta_3 \tan(\theta_4+\theta_5)} + \frac{R_{\text{on}} - j\omega L_s}{R_{\text{on}}^2 + \omega^2 L_s^2} \tag{8}$$

The resonant frequency of the resonator at this point can be determined from $\text{Im}(Y_{\text{ino2}}) = 0$, $\text{Im}(Y_{\text{ine2}}) = 0$. The effects of the lengths of l_3 and l_5 on the two resonant modes of the resonator are shown in Fig. 7. It can be found that the resonant frequency of the resonator changes dramatically due to the change of the input admittances when diodes D_1 and D_2 change from reverse-bias to forward-bias. Fig. 8 illustrates the S-parameters of the proposed initial switchable filter in both operating states (BPF and ASF). It can be seen that the DMR detunes near 2.45 GHz and generates a parasitic passband around 4.2 GHz due to the change of resonant frequency in the ASF state.

2.2. Analysis of Absorption Network

As shown in Fig. 9, the absorption network consists of two $\lambda/4$ parallel coupled lines and an absorption resistor. According to the microwave network and circuit theory, the input impedance Z_{in} of the absorption network is

$$Z_{\text{in}} = \frac{AZ_{\text{TL}} + B}{CZ_{\text{TL}} + D} \tag{9}$$

where A, B, C, and D are the $ABCD$-parameters of $\lambda/4$ parallel coupled lines with odd- and even-mode characteristic impedances of Z_{o1} and Z_{e1}. Its value can be calculated based on [21] as

$$\begin{bmatrix} A & B \\ C & D \end{bmatrix} = \begin{bmatrix} \frac{2(\cos^2\theta_7+1)-\sin^2\theta_7(Z_{e1}/Z_{o1}+Z_{o1}/Z_{e1})}{4\cos\theta_7} & j\frac{(Z_{e1}+Z_{o1})\sin\theta_7}{2Z_{e1}Z_{o1}} \\ j\frac{(Z_{e1}+Z_{o1})\sin\theta_7}{2} & \cos\theta_7 \end{bmatrix} \tag{10}$$

Next, Z_{TL} can be calculated as

$$Z_{\text{TL}} = \frac{A_1 R_2 + B_1}{C_1 R_2 + D_1} \tag{11}$$

where A_1, B_1, C_1, and D_1 are the $ABCD$-parameters of $\lambda/4$ parallel coupled lines with odd- and even-mode characteristic impedances of Z_{o2} and Z_{e2}.

$$\begin{bmatrix} A_1 & B_1 \\ C_1 & D_1 \end{bmatrix} = \begin{bmatrix} \frac{2(\cos^2\theta_8+1)-\sin^2\theta_8(Z_{e2}/Z_{o2}+Z_{o2}/Z_{e2})}{4\cos\theta_8} & j\frac{(Z_{e2}+Z_{o2})\sin\theta_8}{2Z_{e2}Z_{o2}} \\ j\frac{(Z_{e2}+Z_{o2})\sin\theta_8}{2} & \cos\theta_8 \end{bmatrix} \tag{12}$$

Applying Equations (10)–(12) to Equation (9), the input impedance Z_{in} of the absorption network at the center frequency f_0 is

$$Z_{\text{in}} = \infty \tag{13}$$

Then, the reflection coefficient S_{11} of the absorption network can be expressed as

$$S_{11} = \frac{Z_{\text{in}} - Z_{\text{A}}}{Z_{\text{in}} + Z_{\text{A}}} \tag{14}$$

where Z_{A} is the port impedance. According to Equations (13) and (14), it is found that the absorption network is equivalent to an open circuit at the center frequency ($S_{11} = 1$ at f_0), which implies that the odd- and even-mode characteristic impedances of the two parallel coupled lines do not affect the characteristics of the proposed absorption network at f_0.

The reflection coefficient $|S_{11}|$ with different coupling coefficients is given in Fig. 10(a) to analyze the effect of the coupling coefficient on the performances of the absorption network. The coupling coefficient k_1 for the first parallel coupled line is defined as $k_1 = (Z_{e1} - Z_{o1})/(Z_{e1} + Z_{o1})$, and the coupling coefficient k_2 for the second parallel coupled line is defined as $k_2 = (Z_{e2} - Z_{o2})/(Z_{e2} + Z_{o2})$. It can be seen from Fig. 10(a) that the coupling coefficients k_1 and k_2 only affect the BW and the location of the reflection zeros and do not affect the out-of-band absorption. Therefore, the reflectionless bandwidth of the absorption network can be controlled by adjusting the coupling coefficient to fit the filtering bandwidth of the proposed switchable filter.

In order to analyze the effect of absorption resistor R_2, Fig. 10(b) plots the three cases with different $R_2 (Z_{e1} = Z_{e2} =$
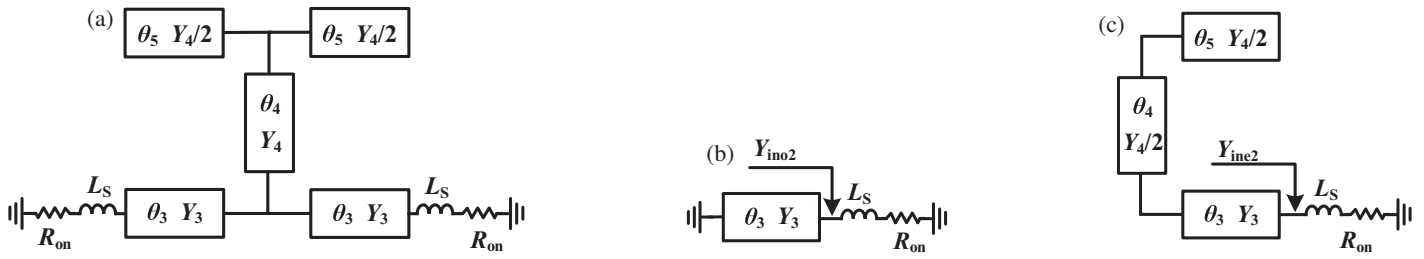
FIGURE 6. (a) Schematic of the resonator with forward-biased diodes. (b) Odd-mode excitation. (c) Even-mode excitation.
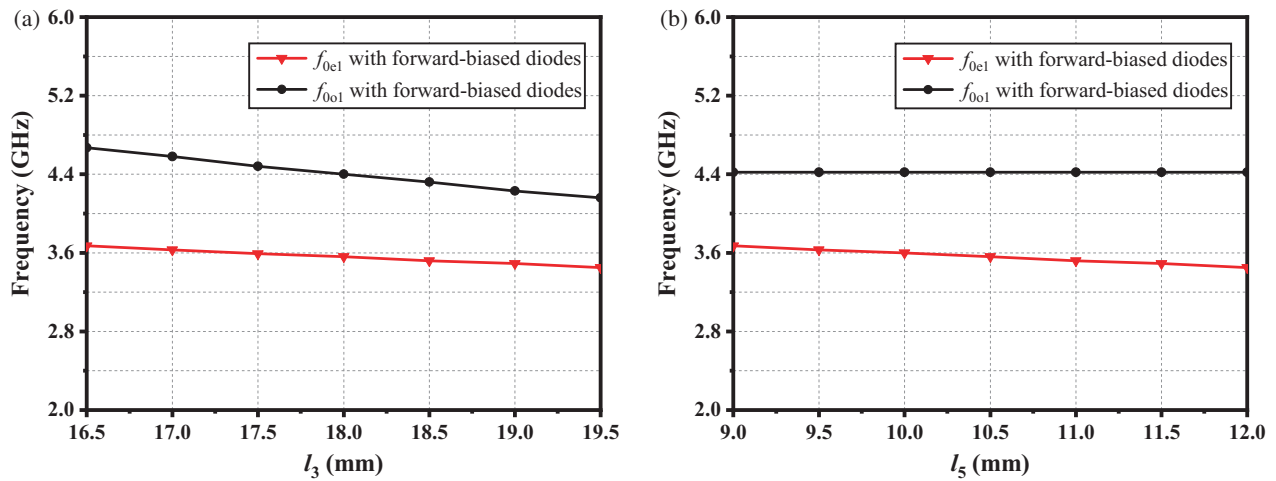

FIGURE 7. Effect of (a) l_3 and (b) l_5 on the odd- and even-mode resonant frequencies of DMR loaded with forward-biased diodes.
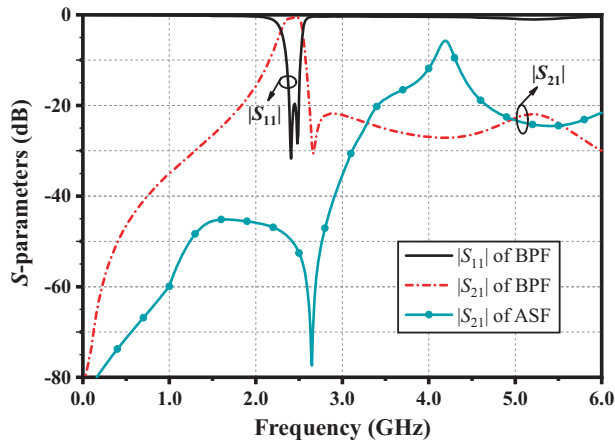

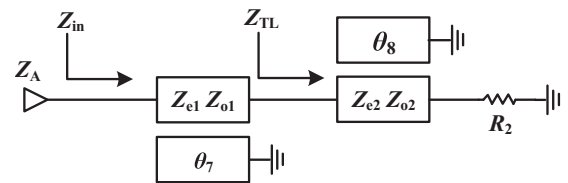FIGURE 8. S-parameters of the proposed initial switchable filter.

FIGURE 9. Circuit schematic of the absorption network.

oughly in the previous sections. Two identical absorption networks loaded at the end of the open stubs of the feeding lines achieve dual-port reflectionless behavior. An open stub with the length of l_6 is loaded on the feeding line to suppress the harmonics in the all-stop state. Table 1 gives the truth table for the switchable filter in both states. The detailed analysis will be expanded below.

$77.46\,\Omega$, $Z_{o1} = Z_{o2} = 46.48\,\Omega$, $k_1 = k_2 = 0.25$, and $Z_A = 50\,\Omega$). It can be seen that as R_2 increases from $50\,\Omega$ to $70\,\Omega$, the two reflection zeros move toward the center frequency $f_0 = 2.45\,\text{GHz}$. The $|S_{11}|$ near 1 GHz and 4 GHz improves, but the $\|S_{11}\|$ near 2 GHz and 3 GHz get worse. Therefore, there is a trade-off for out-of-band absorption by choosing an appropriate value of R_2.

2.3. Analysis of RBPF to ASF

The layout of the proposed bandpass-to-all-stop switchable absorptive filter is given in Fig. 11. The design of the BPF and the analysis of the absorption network have been explained thor-

TABLE 1. Truth table of operation states of the proposed bandpass-to-all-stop switchable absorptive filter.

V_{bias}	DMR	Open stub l_6	Filter state
$-15\,\text{V}$	Enable	Disable	RBPF
$15\,\text{V}$	Disable	Enable	ASF

The state of the filter is RBPF when V_{bias} is $-15\,\text{V}$. The dimensions of each part are optimized based on theoretical analysis. Fig. 12 shows the simulated reflection coefficients S_{11} of the BPF filtering network and absorption network. An ultra-wideband range of reflectionless behavior can be obtained for
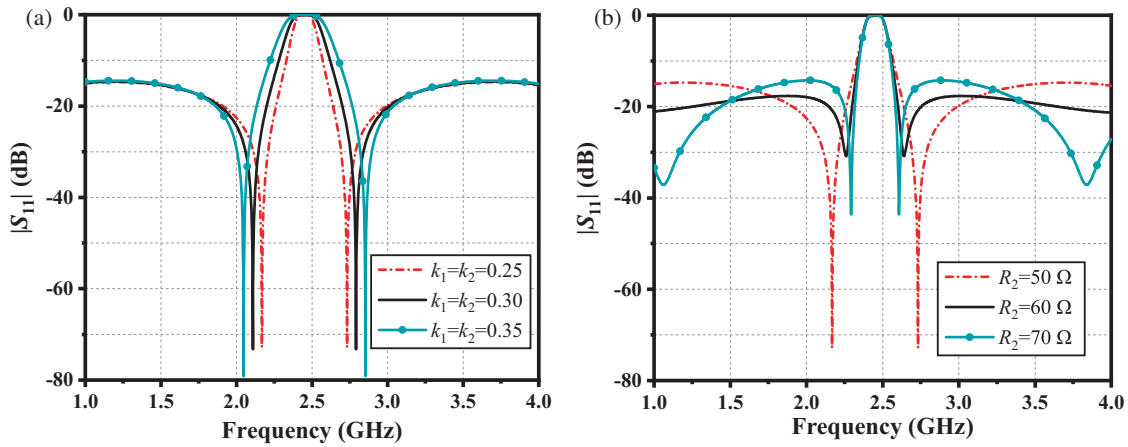
FIGURE 10. (a) Effects of the coupling coefficient on the S_{11} of the absorption network with $\sqrt{Z_{e1}Z_{o1}} = 60\,\Omega$, $\sqrt{Z_{e2}Z_{o2}} = 60\,\Omega$, $Z_A = 50\,\Omega$ and $R_2 = 50\,\Omega$. (b) Effects of the absorption resistor R_2 on the S_{11} of the absorption network with $\sqrt{Z_{e1}Z_{o1}} = 60\,\Omega$, $\sqrt{Z_{e2}Z_{o2}} = 60\,\Omega$, $k_1 = k_2 = 0.25$, $Z_A = 50\,\Omega$.
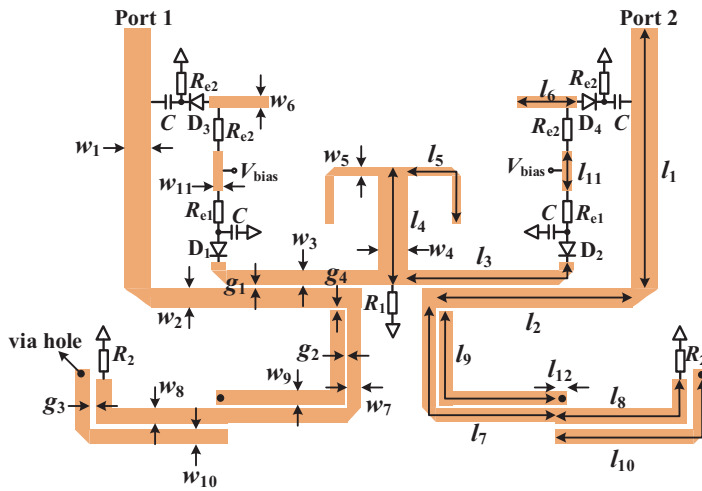

FIGURE 11. Layout of the proposed bandpass-to-all-stop switchable absorptive filter.
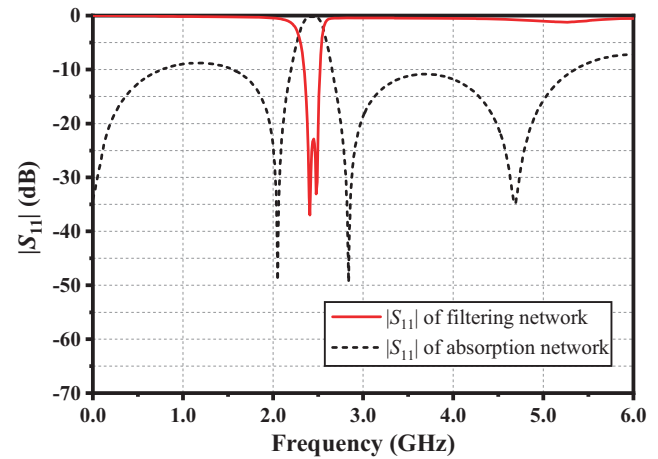

FIGURE 12. Complementary $|S_{11}|$ of filtering network and absorption network.

the BPF since the designed BPF and absorption network exhibit complementary characteristics. Fig. 13 shows a comparison of S-parameters for the filter with and without absorption networks. It can be seen that after loading the absorption network, the passband selectivity is improved; the out-of-band suppression is increased to over 30 dB; and the RL is better than 10 dB over an ultra-wideband range. Fig. 14 compares the S-parameters of the filter with double absorption network (DAN) respectively loaded on the left and right feeding lines and single absorption network (SAN) only loaded on the left feeding line. It can be observed that the filter with double absorption networks has better out-of-band suppression and reflectionless performance.

The state of the filter is ASF when PIN diodes D_1 and D_2 are forward-biased. In order to improve the out-of-band rejection level of the ASF open stubs with the length of l_6 are loaded at a suitable location on the feeding lines to suppress the parasitic passband around 4.2 GHz. A switching circuit is used to enable or disable the open stubs. The current limiting re-

sistor $R_{e2} = 1\,k\Omega$ together with the external bias voltage V_{bias} controls the on/off behavior of PIN diodes D_3 and D_4. Diodes D_3 and D_4 are reverse-biased when the filter is in the RBPF state, and the open stubs are disconnected to minimize the effect on the reflectionless performance. When the filter is in the ASF state, diodes D_3 and D_4 are forward-biased. As shown in Fig. 15, the rejection of the ASF near 2.45 GHz and 4.2 GHz improves significantly with the open stubs.

2.4. Design Procedure

Based on the above analysis, the design process of the proposed bandpass-to-all-stop switchable absorptive filter can be summarized as follows.

1) Determine the design scheme of the switchable filter, which realizes the switching of the BPF and ASF by loading PIN diodes at the end of the DMR.

2) Determine the desired center frequency f_0, BW, and RL of the BPF, and synthesize the coupling matrix. Adjust θ_3, θ_4, and
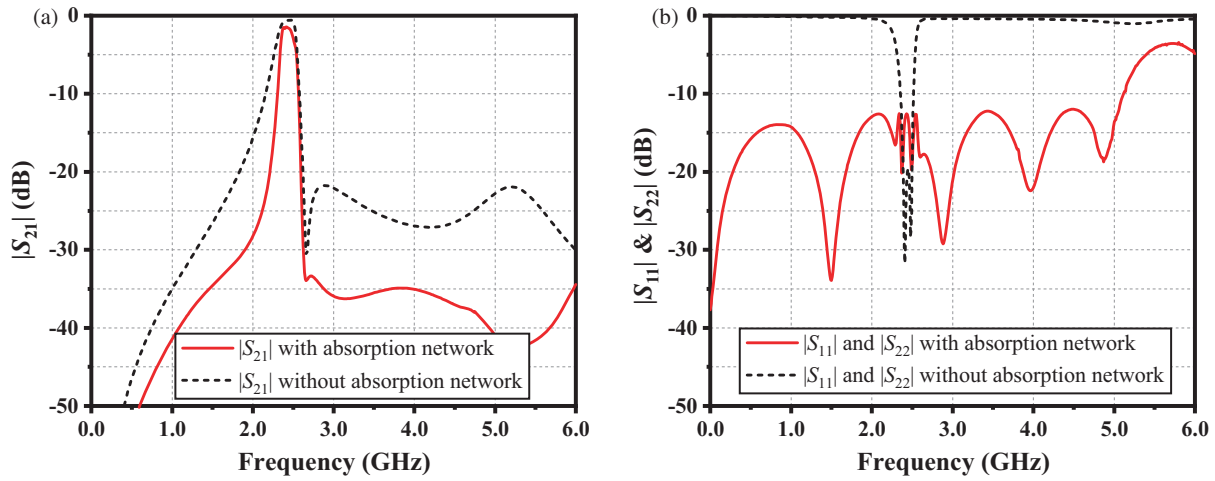
FIGURE 13. Simulated responses of the filter with and without absorption network. (a) $|S_{21}|$. (b) $|S_{11}|$ and $|S_{22}|$.
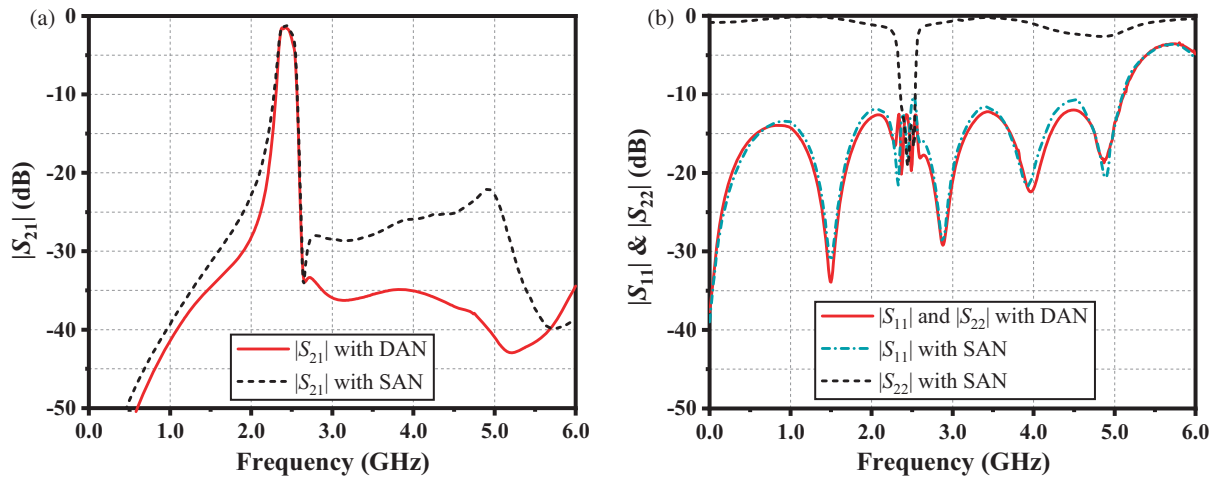

FIGURE 14. Simulated responses of the filter with double and single absorption networks. (a) $|S_{21}|$. (b) $|S_{11}|$ and $|S_{22}|$.
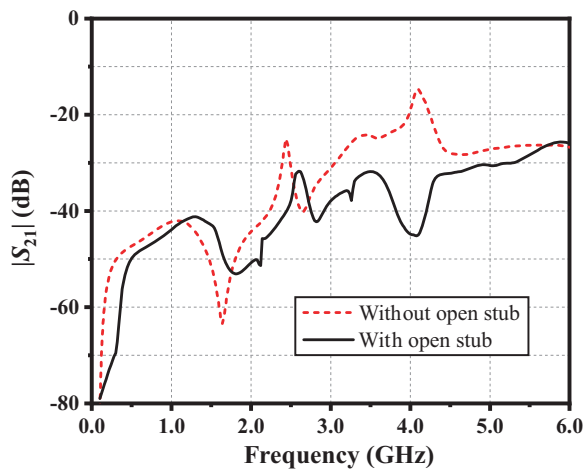

FIGURE 15. Simulated performances of the ASF with or without open stub.

FIGURE 16. Photograph of the proposed bandpass-to-all-stop switchable absorptive filter with an ultra-wideband reflectionless range.

θ_5 of the DMR and its impedance to satisfy the odd-mode and even-mode resonant frequencies f_{0o1} and f_{0e1}. Adjust the feeding lines and th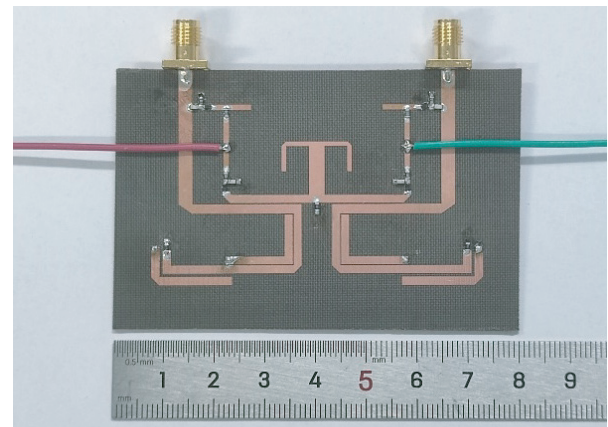e coupling gap between the feeding line and the resonator to satisfy the external quality factor Q_e. A grounding resistor R_1 is connected to the resonator to suppress even harmonics.
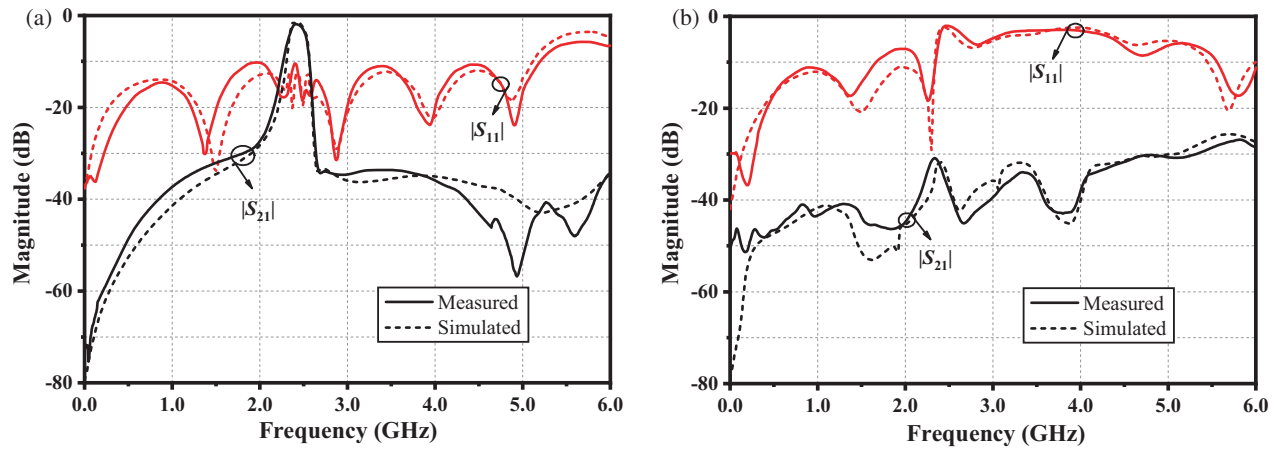
FIGURE 17. Simulated and measured results of the proposed bandpass-to-all-stop switchable absorptive filter with an ultra-wideband reflectionless range. (a) RBPF state. (b) ASF state.

TABLE 2. Comparison with related references.

References	f_0 (GHz)	Absorptive Behavior	10-dB Reflectionless FBW (%)	IL (dB)	Upper Stopband (Rejection Level)	Switchable
[18]	1.3~2	Single-port	<90	0.96	<$1.56 f_0$ (>20 dB)	Yes
[19]	2	Single-port	61.9	2		Yes
[22]	2.11~2.72	Single-port	<71.6	4	<$1.66 f_0$ (>30 dB)	No
[23]	2	Single-port	<74	1.43	<$1.50 f_0$ (>28 dB)	No
[24]	1.97	Dual-port	130	0.71		No
[25]	0.7	Dual-port	102.6	4	<$1.71 f_0$ (>23 dB)	Yes
This work	**2.43**	**Dual-port**	**214**	**1.92**	**<$2.45 f_0$ (>33 dB)**	**Yes**

3) According to Fig. 10, select the coupling coefficients k_1 and k_2 of the two parallel coupling lines in the absorption network to match the bandwidth of the BPF, and choose the values of the absorption resistor R_2 to obtain a good reflectionless performance.

4) Optimize the rejection in the ASF state by connecting open stubs in parallel at suitable locations on the feeding lines.

5) The physical dimensions are further optimized using the electromagnetic simulation software ANSYS HFSS. Manufacture the prototype and measure it using an Agilent N5230A network analyzer.

3. SIMULATED AND MEASURED RESULTS

The overall size of the bandpass-to-all-stop switchable absorptive filter with an ultra-wideband reflectionless range is $0.605\lambda_g^2$, where λ_g is the guided wavelength at 2.45 GHz. The filter prototype is designed and fabricated on an F4B substrate with a thickness of 1 mm, relative permittivity of 2.65, and loss tangent of 0.003. SMP1345-079LF PIN diodes were used. The optimized physical dimensions are as follows: $l_1 = 26.58$, $l_2 = 20.08$, $l_3 = 17.13$, $l_4 = 12.11$, $l_5 = 9.97$, $l_6 = 7.8$, $l_7 = 23.28$, $l_8 = 15.73$, $l_9 = 19.8$, $l_{10} = 20.23$, $l_{11} = 10.95$, $l_{12} = 1$, $w_1 = 2.65$, $w_2 = 1.85$, $w_3 = 1.55$, $w_4 = 3$, $w_5 = 0.87$, $w_6 = 1$, $w_7 = w_9 = 1.5$, $w_8 = w_{10} = 1.55$, $w_{11} = 1.0$, $g_1 = 0.25$, $g_2 = 0.25$, $g_3 = 0.7$, $g_4 = 0.3$ (unit: mm). The diameter of the metal via hole is set to 0.5 mm.

Other circuit element values are set as follows: $C = 100\,\text{pF}$, $R_{e1} = 2\,\text{k}\Omega$, $R_{e2} = 1\,\text{k}\Omega$, $R_1 = R_2 = 50\,\Omega$. Fig. 16 shows a photograph of the fabricated bandpass-to-all-stop switchable absorptive filter with an ultra-wideband reflectionless range, and Fig. 17 plots the simulated and measured results, which are in good agreement.

When $V_{\text{bias}} = -15\,\text{V}$, the switchable filter is in RBPF state. As shown in Fig. 17(a), the measured 3-dB fractional bandwidth (FBW) is 8.23% from 2.33 to 2.53 GHz with a center frequency of 2.43 GHz. The minimum IL within the passband is 1.92 dB, and the RL is better than 10 dB from to 5.2 GHz with ultra-wideband reflectionless FBW of 214%. Besides, RBPF exhibits out-of-band rejection of over 33 dB and wide stopband characteristics with an upper stopband reaching up to 6 GHz. When $V_{\text{bias}} = 15\,\text{V}$, the switchable filter is in ASF state, and the simulation and measurement results are shown in Fig. 17(b). The rejection level in the ASF state is better than 30 dB from 0 to 5.32 GHz and better than 26.9 dB over the entire measured frequency range.

Table 2 gives a performance comparison with some related references. The proposed bandpass-to-all-stop switchable absorptive filter achieves an ultra-wideband 10-dB reflectionless FBW of 214%. Upper stopband rejection better than 33 dB reaches up to $2.45 f_0$ in the RBPF state, which is superior to other references. In addition, dual-port reflectionless behavior and functional switchability are implemented (ASF state).

4. CONCLUSION

In this paper, a novel bandpass-to-all-stop switchable absorptive filter with an ultra-wideband reflectionless range has been proposed. An ultra-wide reflectionless range is realized by loading an absorption network consisting of parallel coupled lines and absorption resistors at the end of the open stubs of feeding lines. PIN diodes are utilized to switch the filter state. The design process is thoroughly analyzed, and the simulation and measurement results show good consistency. Measurement results show that the proposed switchable filter can realize the switching from RBPF to ASF, and the RBPF has an ultra-wide reflectionless range and excellent out-of-band rejection characteristics.

ACKNOWLEDGEMENT

REFERENCES

[1] Guan, X., H. Su, H. Liu, P. Wen, W. Liu, P. Gui, and B. Ren, "Miniaturized high temperature superconducting bandpass filter based on D-CRLH resonators," *IEEE Transactions on Applied Superconductivity*, Vol. 29, No. 5, 1–4, Aug. 2019.

[2] Li, D. and K.-D. Xu, "Multifunctional switchable filter using coupled-line structure," *IEEE Microwave and Wireless Components Letters*, Vol. 31, No. 5, 457–460, May 2021.

[3] Sun, Z., X. Wang, and K. Li, "A switchable bandpass filter for broadband, dual-band and tri-band operations," *IEEE Transactions on Circuits and Systems II: Express Briefs*, Vol. 70, No. 1, 111–115, Jan. 2022.

[4] Yan, Z., X. Zhang, X. He, Y. Ye, B. Hou, C. Hu, and W. Wen, "A high performance dual-band switchable bandpass filter and its application in 5G signal detector," *IEEE Transactions on Components, Packaging and Manufacturing Technology*, Vol. 13, No. 8, 1242–1253, Aug. 2023.

[5] Chan, K. Y., R. Ramer, and R. R. Mansour, "A switchable iris bandpass filter using RF MEMS switchable planar resonators," *IEEE Microwave and Wireless Components Letters*, Vol. 27, No. 1, 34–36, Jan. 2017.

[6] Xu, J., Q.-H. Cai, Y.-F. Guo, S.-Y. Ji, and Y.-W. Duan, "A BPF integrated SP4T switch using parallel switched fractal common feeding line," *IEEE Transactions on Circuits and Systems II: Express Briefs*, Vol. 68, No. 6, 1932–1936, Jun. 2021.

[7] Cho, Y.-H., C. Park, and S.-W. Yun, "0.7–1.0-GHz switchable dual-/single-band tunable bandpass filter using a switchable J-inverter," *IEEE Access*, Vol. 9, 16 967–16 974, 2021.

[8] Chen, X., Y. Wu, Y. Yang, and W. Wang, "Simple coupled-line tunable bandpass filter with wide tuning range," *IEEE Access*, Vol. 8, 82 286–82 293, 2020.

[9] Wu, X., Y. Li, and X. Liu, "High-order dual-port quasi-absorptive microstrip coupled-line bandpass filters," *IEEE Transactions on Microwave Theory and Techniques*, Vol. 68, No. 4, 1462–1475, Apr. 2020.

[10] Zhu, Y., J. Cai, W. Qin, W. Yang, and J. Chen, "Compact input-reflectionless balanced bandpass filter with flexible bandwidth using three-line coupled structure," *Frontiers of Inform. Tech. & Electronic Engineering*, Vol. 24, No. 2, 314–326, 2023.

[11] Gómez-Garcia, R., J.-M. Muñoz-Ferreras, and D. Psychogiou, "High-order input-reflectionless bandpass/bandstop filters and multiplexers," *IEEE Transactions on Microwave Theory and Techniques*, Vol. 67, No. 9, 3683–3695, Sep. 2019.

[12] Xu, K.-D., S. Lu, Y.-J. Guo, and Q. Chen, "Quasi-reflectionless filters using simple coupled line and T-shaped microstrip structures," *IEEE J. of Radio Freq. Identification*, Vol. 6, 54–63, 2021.

[13] Lee, S. and J. Lee, "Accurate synthesis of input-reflectionless dual-passband filter," *IEEE Transactions on Microwave Theory and Techniques*, Vol. 71, No. 3, 1148–1158, Mar. 2023.

[14] Zhang, Y., Y. Wu, W. Wang, and J. Yan, "High-performance common-and differential-mode reflectionless balanced bandpass filter using coupled ring resonator," *IEEE Trans. on Circuits and Syst. II: Express Briefs*, Vol. 69, No. 3, 974–978, Mar. 2022.

[15] Zhao, X.-B., F. Wei, L. Yang, and R. Gómez-García, "Two-layer-magic-t-based bandpass, quasi-bandstop, and dual-passband balanced filters with differential-/common-mode reflectionless behavior," *IEEE Transactions on Microwave Theory and Techniques*, Vol. 72, No. 4, 2267–2282, Apr. 2024.

[16] Fan, M., K. Song, L. Yang, and R. Gómez-García, "Frequency-tunable constant-absolute-bandwidth single-/dual-passband filters and diplexers with all-port-reflectionless behavior," *IEEE Transactions on Microwave Theory and Techniques*, Vol. 69, No. 2, 1365–1377, Feb. 2021.

[17] Jeong, S.-W., T.-H. Lee, and J. Lee, "Frequency- and bandwidth-tunable absorptive bandpass filter," *IEEE Trans. on Microwave Theory and Techniques*, Vol. 67, No. 6, 2172–2180, Jun. 2019.

[18] Gómez-García, R., J.-M. Muñoz-Ferreras, and D. Psychogiou, "Dual-behavior resonator-based fully reconfigurable input reflectionless bandpass filters," *IEEE Microwave and Wireless Components Letters*, Vol. 29, No. 1, 35–37, Jan. 2019.

[19] Wu, H., G. Wu, and J. Shi, "Design of a switchable reflectionless filter with bandpass and bandstop modes," in *2023 IEEE International Workshop on Electromagnetics: Applications and Student Innovation Competition (iWEM)*, 227–229, Harbin, China, 2023.

[20] Hong, J.-S. G. and M. J. Lancaster, *Microstrip Filters for RF/Microwave Applications*, John Wiley & Sons, 2004.

[21] Zysman, G. I. and A. K. Johnson, "Coupled transmission line networks in an inhomogeneous dielectric medium," *IEEE Transactions on Microwave Theory and Techniques*, Vol. 17, No. 10, 753–759, Oct. 1969.

[22] Fan, M., K. Song, L. Yang, and R. Gómez-Garcia, "Frequency-reconfigurable input-reflectionless bandpass filter and filtering power divider with constant absolute bandwidth," *IEEE Transactions on Circuits and Systems II: Express Briefs*, Vol. 68, No. 7, 2424–2428, Jul. 2021.

[23] Feng, W., X. Ma, Y. Shi, S. Shi, and W. Che, "High-selectivity narrow-and wide-band input-reflectionless bandpass filters with intercoupled dual-behavior resonators," *IEEE Transactions on Plasma Science*, Vol. 48, No. 2, 446–454, Feb. 2020.

[24] Luo, C., S.-W. Wong, J.-Y. Lin, Y. Yang, Y. Li, X.-Z. Yu, L.-P. Feng, Z.-H. Tu, and L. Zhu, "Quasi-reflectionless microstrip bandpass filters using bandstop filter for out-of-band improvement," *IEEE Transactions on Circuits and Systems II: Express Briefs*, Vol. 67, No. 10, 1849–1853, Oct. 2020.

[25] Zhang, Z. and D. Psychogiou, "Multifunctional bandpass filter with codesigned tunable attenuator and reflectionless phase shifter functionalities," *IEEE Microwave and Wireless Technology Letters*, Vol. 34, No. 6, 737–740, Jun. 2024.